Incommensurate phases of a supported nanoparticle film subjected to uniaxial compression

Yenchao Chua[a], Brian Leahy[b], Minke Zhang[a], Siheng You[a], Ka Yee C. Lee[a,c], Susan N. Coppersmith[d,1], and Binhua Lin[a,b]

[a]James Franck Institute, [b]Center for Advanced Radiation Sources, and [c]Department of Chemistry and Institute for Biophysical Dynamics, University of Chicago, Chicago, IL 60637; and [d]Department of Physics, University of Wisconsin-Madison, Madison, WI 53706

We investigate experimentally and theoretically the sequence of phases that occurs when a self-assembled monolayer of gold nanoparticles supported on a fluid is compressed uniaxially in a Langmuir trough. Uniaxial compression of the monolayer results in the appearance of lines that have been shown to be regions of trilayer. These lines exhibit complex patterns that depend on the extent of compression. We show that these patterns can be understood in terms of an equilibrium statistical mechanical theory, originally developed in the context of commensurate–incommensurate transitions in krypton monolayers adsorbed on graphite, in which there is an energy cost to line deformations and to line intersections. Even though line intersections are energetically costly, they lower the free energy because they cause the entropy of the system to increase when the density of lines is low enough. Our analytic and Monte Carlo analyses of the model demonstrate that the model exhibits two-phase coexistence. Our experimental observations are qualitatively consistent with the predictions of the model.

pattern formation | two-dimensional phase transitions

The collapse behavior of nanometer- and molecular-thin films at interfaces has fascinated researchers for decades (1, 2). In particular, methods of producing patterns at length scales significantly above the size of the constituent particles have recently garnered interest (3, 4). Most previous work has focused on structures that can be understood via a one-dimensional approach (5–7), especially highly ordered structures (8–10). In this report, we examine a different, 2D pattern observed on a self-assembled solid monolayer of gold nanoparticles that is in a metastable state. Under uniaxial compression, the film buckles into localized areas of trilayer coexisting with the monolayer, forming a complex "hash" network across the surface of the film (11). We examine the global arrangement of the buckled hash network on the surface, using statistical mechanical arguments. Our theory and experiment both show a disordered hexagonal arrangement of the trilayer areas. This type of pattern may be present on other films that collapse repeatedly into multilayers and are sufficiently influenced by thermal fluctuations, such as in biological (12, 13) or Langmuir films (14, 15). It should be noted that these patterns may not be visually discernable. We demonstrate that there is a theoretical similarity between collapse structure in these films and the well-studied commensurate–incommensurate (C-I) transition in molecules adsorbed on crystalline solids (16–26). This similarity manifests itself in the structural arrangement of the hash lines of the nanoparticle trilayer, forming the same liquid hexagonal phase observed in molecules adsorbed on periodic substrates (27).

In the experiments reported here, a nanoparticle film is formed by spreading a solution of 6-nm (11, 28) Au nanoparticles ligated with dodecanethiol at the air–water interface in a Langmuir trough. As the solvent droplet evaporates, the film condenses into solid monolayer domains separated by regions of open air–water interface (11, 28). The monolayer is then compressed uniaxially in the plane of the interface in the x-direction by two moving barriers, while confined in the in-plane y-direction by the borders of the trough (see Fig. S1 for schematics of the apparatus and the coordinates). The

film is free to buckle out-of-plane in the z-direction into the subphase or superphase. Details about the experimental setup and apparatus have previously been published (11). Upon compression, the film buckles, forming localized trilayer regions surrounded by a monolayer (11, 28). Whereas one might intuitively expect the solid film to buckle in a straight, one-dimensional striped pattern determined by the direction of compression, we instead observe an orientation of the trilayer regions into a fully 2D pattern of lines (11). In this report, we focus on the large-scale organization of these lines as the degree of compression increases.

For small compressions (Fig. 1A: trilayer coverage of 4.2%), the lines form a disordered intersecting network, denoted as an intermediate hash stage. As compression is increased and the density of trilayer lines increases (Fig. 1B: trilayer coverage of 46.4%), the configuration changes significantly and becomes more anisotropic, and regions of very closely spaced lines appear. Here we address basic questions about these configurations and their evolution, in particular (i) why the lines form trilayer hash instead of an aligned array of nonintersecting lines at low density and (ii) why the lines become more oriented and form regions of very high density as their overall density increases. We propose that insight into the experimental results can be obtained by considering a theoretical model in which lines that can meander and also intersect are assumed to achieve thermodynamic equilibrium. In such a model, line intersections can lower the free energy because they increase the system's entropy, even if they are energetically costly.

The theoretical model that we investigate is closely related to models that have been studied previously to model C-I transitions of molecules adsorbed on periodically corrugated substrates (16–26, 29). Using analytic arguments and Monte Carlo simulations, we show that at low density the model exhibits a disordered phase that can be viewed as a hexagonal array with dislocations (16, 17), whereas at high density there is a two-phase coexistence of the disordered hexagonal phase with a very high density of parallel lines. That the disordered hexagonal phase was favored at low enough density was pointed out in refs. 16 and 17, but the presence of the substantial region of two-phase coexistence has not been realized previously. The behavior obtained theoretically is in good qualitative agreement with experimental observations.

The success of the theory in describing the qualitative trends in the experiment is remarkable in view of the fact that direct observation of the experimental system does not yield evidence for significant relaxation on experimental timescales. The success of the entropic mechanism investigated in this paper in describing several different aspects of the experimentally observed behavior
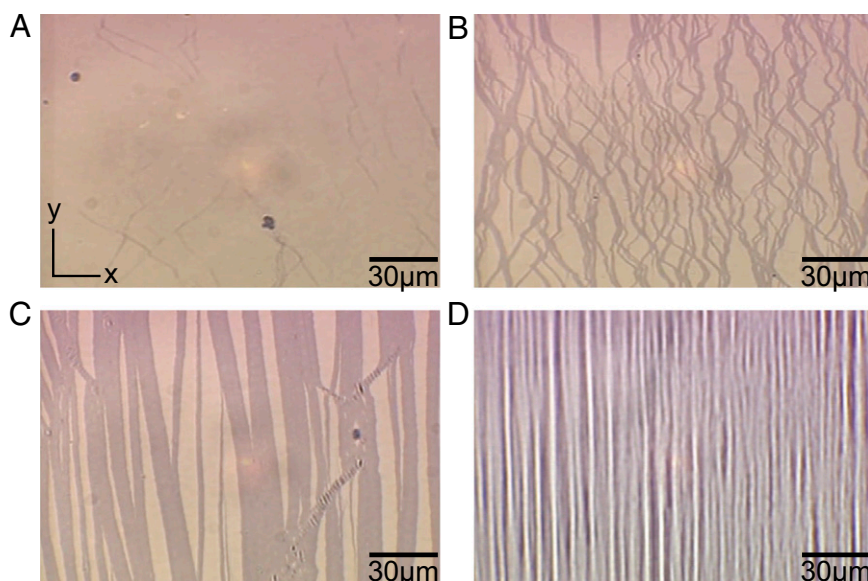
Fig. 1. Typical metastable configurations of the system undergoing compression. Under a relatively small degree of compression (trilayer coverage of 4.2%), the configuration in *A* appears, showing a few trilayer lines. (*B*) After further compression (trilayer coverage of 46.4%), lines with significant wandering and intersection appear, as the film enters the intermediate "hash" stage. As compression continues, the configuration transforms into *C* (trilayer coverage of 68.9%), showing the congregation of hash lines into thick bands. (*D*) Further compression after the film becomes a uniform trilayer causes it to wrinkle. The trilayer coverage is determined by calculating the coverage of the darkened areas (trilayer) relative to the whole picture.

suggests that significant configurational relaxation occurs in the initial stages of the formation of the pattern.

Theoretical Model

The model that we apply to the experiment is a phenomenological one formulated in terms of the lines of trilayer. We take it as a given that the compression causes the formation of these lines to be energetically favored and that the density of lines is fixed because it is determined by the degree of compression. The free energy for the system is then written in terms of the properties of these lines. This approach has been applied successfully to the study of C-I transitions in systems with charge-density waves (18, 30, 31) and in adsorbed rare gas monolayers on periodic substrates (16–26). The lines have an energy per unit length ϵ_ℓ that depends on the degree of compression (ϵ_ℓ is positive for small enough compression and decreases as the compression is increased), and each line intersection or vertex costs energy E_V. Therefore, the total energy, E, of the system is

$$E = \epsilon_\ell L + E_V N_V, \qquad [1]$$

where L is the total length of lines summed and N_V is the number of vertices. It is important to note that this energy function is independent of any sort of underlying structure (lattice, etc.).

The fact that there is a parameter region in which the density of lines is low is evidence that the vertex energy $E_V > 0$, because if E_V were negative, then the C-I transition would be strongly first order. Indeed, it is quite plausible intuitively that the energy cost of a line intersection in our system is positive. For example, vertex interactions between folded ridges have been found to increase the strain energy (32). Therefore, we expect that the configurations of lines in our experimental system are all in the regime $\epsilon_\ell < 0, E_V > 0$.

If the energy cost of line intersections is positive, then one might think that it would be favorable for the line configurations to have no intersections, which is possible if the lines are roughly parallel, in a "striped" configuration (18, 21, 22). If line intersections are energetically costly, then there is an entropically induced repulsion between the lines—essentially, a line has less freedom to wander when it is near a neighbor, because of the "danger" that a fluctuation would cause an intersection (22, 23), and it is natural to

expect the configurations to consist of lines that are well separated from each other. However, Villain (24) pointed out that even if line intersections are energetically costly, the entropy of a hexagonal phase is large enough that at low enough density it has lower free energy at any nonzero temperature. The additional entropy of the hexagonal array is illustrated in Fig. 2: the three configurations shown all have the same energy because they all have the same length of line and number of intersections. The entropy per unit area of the hexagonal phase is $\ln(\ell/a)/\ell^2$, where ℓ is the average hexagon side length and a is a microscopic length setting the minimum spatial variation scale (16, 17, 24). Because the energy cost per unit area of intersections is proportional to $1/\ell^2$, the entropic contribution [which is proportional to $\ln(\ell/a)/\ell^2$] dominates when ℓ is large enough [an ℓ large enough that $k_B T \ln(\ell/a)/\ell^2 > \beta E_V/\ell^2$, where β is a numerical factor, and not the inverse temperature $\frac{1}{k_B T}$] and the hexagonal phase has lower free energy than the striped phase in the limit $\ell \to \infty$ (note that the $1/\ell$ term is irrelevant here because the total number of particles is fixed; see *SI Text S1* for proof).

Therefore, the free energy per unit area of the hexagonal phase, f_H, is (16, 17, 24)

$$f_H = \frac{\alpha \epsilon_\ell}{\ell} + \frac{\beta E_V}{\ell^2} - \frac{k_B T}{\ell^2} \ln\left(\frac{\ell}{a}\right), \qquad [2]$$
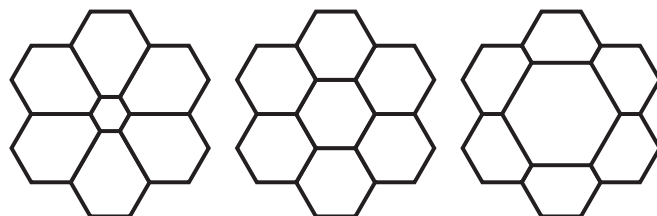

Fig. 2. Schematic illustration of entropy of the hexagonal array when hexagon angles are 60°. The energies of the three configurations are identical, because the total length of line and the number of intersections are the same. Because of this entropy, the hexagonal phase has lower free energy than the striped phase at nonzero temperature when the line density is low enough.

where α and β are numerical factors of order unity determined by the geometry. Note that when $\epsilon_\ell \leq 0$, the free energy is negative as $\ell \to \infty$.

The free energy per unit area of the striped phase, f_S, when the mean line separation is λ, is (22, 23)

$$f_S = \frac{\gamma \epsilon_\ell}{\lambda} + \frac{\eta k_B T}{\lambda^3}, \qquad [3]$$

where γ and η are numerical factors. The second term in Eq. **3** is contributed by an effective interaction between the lines $\propto 1/\lambda^3$ that arises because of entropic effects (22, 23). When $\epsilon_\ell = 0$, the free energy of the striped phase is positive. Therefore, when ϵ_ℓ is just barely negative, the hexagonal phase has lower free energy than the striped phase.

Although the free energy of the ordered hexagonal phase is lower than that of the striped phase, it does not minimize the free energy. Refs. 16 and 17 demonstrate that the free energy can be lowered further by introducing dislocations into the ordered hexagonal phase, so that when the density of lines is very small, the system is in a phase described by a liquid that can be thought of as a melted hexagonal array of domain lines. Here, we characterize the disordered hexagonal phase in more detail, using both Monte Carlo simulations and analytic calculations, with the goal of determining whether its properties are consistent with the hash observed in the nanoparticle films.

Monte Carlo Simulation. We performed Monte Carlo simulations to characterize the thermal equilibrium properties of a model described in Eq. **1**. Many Monte Carlo simulations have been done on systems exhibiting C-I transitions (29, 33–38), but almost all of them explicitly simulate all of the particles, including those that are in the commensurate regions and thus not in the lines, seriously limiting the number of lines that can be simulated when the density of lines is low. Refs. 16 and 17 study the C-I transition using a description formulated entirely in terms of the domain lines between large commensurate regions, but use Monte Carlo simulations that are explicitly restricted to hexagonal arrays with no dislocations. Here, we formulate the problem in terms of artificial "particles" that represent the "excess density" (the nonmonolayer portions of the system). These artificial particles are governed by an energy functional that favors the formation of lines but not line breaking and line intersections while still allowing for topological changes in the line configurations. We do this by writing down a model in which the energetics are chosen so that lines with no intersections have lower energy than other candidate configurations, but broken lines, intersections, and other rearrangements are allowed. Our goal is not to treat the microscopics of the experimental system accurately, but rather to construct a model that has the fundamental scalings of the energetics of lines meandering, intersecting, and dissolving. The model examined here favors linear assemblies of particles as opposed to isolated particles, allows for line intersections with the payment of an energy cost, and allows for topological changes in the arrangement of the lines. The Hamiltonian that we investigate has energy penalties for changes in line direction, for line intersections, and for line terminations, so that the states of lowest energy are those with parallel lines.

The energy functional is described in detail in *Materials and Methods*, *Monte Carlo Simulation*. It is important to not confuse the particles in the simulation with the nanoparticles in the experiment. The particle in the simulation is not a particle per se, but rather a simplified abstraction used in a statistical mechanical computation. To avoid confusion, the term particle always refers to the discrete objects in the simulation and the term "nanoparticle" always refers to the particles in the experiment.

The free energy per unit area in the two-phase region, f_{S+H}, is just the weighted sum of the free energies per unit area of the two phases, f_S and f_H, where f_S is the free energy per unit area of

the striped phase, f_H is the free energy per unit area of the hexagonal phase, and ρ is the fraction of striped phase:

$$f_{S+H} = \rho \left(\frac{\eta k_B T}{\lambda^3} \right) + (1-\rho) \left(\frac{4 E_V}{3\sqrt{3}\ell^2} - \frac{k_B T}{\ell^2} \ln \left(\frac{\ell}{a} \right) \right). \qquad [4]$$

Note that the $1/\lambda$ and $1/\ell$ terms are dropped from Eq. **4** because the total number of particles is fixed (details of the calculation in *SI Text S1*).

Theoretical Results

In this section we first present theoretical results for the Monte Carlo simulations and then those for the analytic calculations.

Results of Simulation. In our Monte Carlo simulations, we investigated the effects of changing the particle density and of changing the parameter E_{010101} that governs the energy cost of vertices. The energy parameters governing clusters of adjacent particles (see Fig. 7 and *Materials and Methods*, *Monte Carlo Simulation* for a detailed explanation) are assumed to be very large because of the large number of particles in the local configuration and therefore are not relevant to the energetic cost of a vertex. As either the particle density or the vertex energy is increased, the configurations observed in the Monte Carlo simulation change in a fashion consistent with the existence of a transition from a disordered hexagonal phase to a two-phase coexistence of hexagons and stripes. Fig. 3 shows two configurations with parameter values $E_{010101} = 15.094$ and $E_{010101} = 20.282$, with the other parameters set to the values $\rho = 0.33$, $\frac{1}{k_B T} = 0.135$, and 60×60 cells and all other parameters as defined in *Materials and Methods*, as well as in Fig. 7. The configurations shown in Fig. 3 are in thermal equilibrium, as verified by checking that their nature does not depend on the choice of initial conditions. Note that the two configurations shown in Fig. 3 have the same energy functional except for E_{010101}, the vertex energy. When the vertex energy is below a critical value, the system is in a disordered hexagonal configuration (Fig. 3*A*). As the vertex energy increases above the critical value, as expected from theoretical analysis, the system exhibits phase coexistence (Fig. 3*B*). Increasing the vertex energy further increases the relative fraction of the stripes compared with the disordered hexagons. In the region in which there is phase coexistence, the striped phase is extremely dense.

Fig. 4 demonstrates that the behavior as the density is increased is qualitatively very similar to that observed when the vertex energy is increased. Taking the configuration in Fig. 4*F* and increasing the particle density from 0.33 to 0.44 yields the configuration of phase coexistence (of lines and disordered hexagons) seen in Fig. 3*B*.

Results of Analytic Calculations. We minimize Eq. **4** with the constraint that the total number of particles must be fixed:

$$\sigma = \rho \frac{\chi}{\lambda} + (1-\rho) \frac{2\chi}{\sqrt{3}\ell}. \qquad [5]$$

Here, χ is the number of particles per unit length of line and σ is the total number of particles per unit area. Thus, we minimize the free energy $\mathcal{F}$ with respect to the parameters ℓ, λ, and ρ:

$$\mathcal{F} = \rho \left(\frac{\eta k_B T}{\lambda^3} \right) + (1-\rho) \left(\frac{4 E_V}{3\sqrt{3}\ell^2} - \frac{k_B T}{\ell^2} \ln \left(\frac{\ell}{a} \right) \right)$$
$$+ \zeta \left(\sigma - \rho \frac{\chi}{\lambda} - (1-\rho) \frac{2\chi}{\sqrt{3}\ell} \right), \qquad [6]$$

where ζ is a Lagrange multiplier. Minimizing Eq. **6** and fixing ζ so that the constraint is satisfied yields the following results:
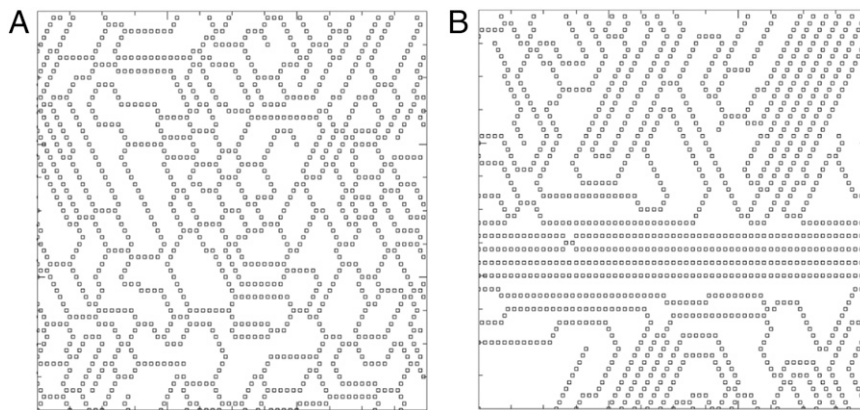
Fig. 3. Particle configurations at different vertex energies. (*A*) Particle configuration when the vertex energy ($E_{010101} = 15.094$) is below the critical value (an explanation of the energy-naming convention is given in *Materials and Methods*). (*B*) Configuration obtained when the vertex energy ($E_{010101} = 20.282$) is above the critical value. All parameters are defined in *Materials and Methods*, and all parameters other than the energy E_{010101} defining the vertex energy are the same in both simulations: Particle density $\rho = 0.33$, $\frac{1}{k_B T} = 0.135$, and 60×60 cells. Both simulations were run for 6×10^8 Monte Carlo steps (MCS).

$$\ell = \frac{54\sqrt{3}\eta k_B T \left(4\sqrt{3}E_V - 9k_B T \left(\ln\left(\frac{\ell}{a}\right) - 1\right)\right)^2}{\left(8\sqrt{3}E_V - 9k_B T \left(2\ln\left(\frac{\ell}{a}\right) - 1\right)\right)^3}, \quad [7]$$

$$\lambda^2 = \frac{2{,}916(\eta k_B T)^2 \left(4\sqrt{3}E_V - 9k_B T \left(\ln\left(\frac{\ell}{a}\right) - 1\right)\right)^2}{\left(8\sqrt{3}E_V - 9k_B T \left(2\ln\left(\frac{\ell}{a}\right) - 1\right)\right)^4}, \quad [8]$$

$$\rho = \frac{\lambda\left(3\ell^2\sigma - 2\sqrt{3}\chi\right)}{\chi\left(3\ell^2 - 2\sqrt{3}\lambda\right)} \to 0 \ \ as \ \ \sigma \to \frac{2\sqrt{3}\chi}{3\ell^2}. \quad [9]$$

Eq. **7** shows that in the two-phase coexistence region the equilibrium value of ℓ is independent of particle density and depends on the external parameters and constants of the system only. Eq. **10** shows that the equilibrium value of λ from Eq. **8** scales with ℓ in the region of two-phase coexistence as

$$\lambda^2 \sim \frac{\left(\ln\left(\frac{\ell}{a}\right) - 2\right)^2}{\left(2\ln\left(\frac{\ell}{a}\right) - 3\right)^4}, \quad [10]$$

which approaches

$$\lim_{\ell \to \infty} \frac{\left(\ln\left(\frac{\ell}{a}\right) - 2\right)^2}{\left(2\ln\left(\frac{\ell}{a}\right) - 3\right)^4} = \frac{1}{\left(\ln\left(\frac{\ell}{a}\right)\right)^2}. \quad [11]$$

This result can be understood qualitatively by noting that the entropic contribution to the free energy per unit area of the hexagonal phase is proportional to $1/\ell^2$, whereas in the striped phase it is proportional to $1/\lambda^3$. Therefore, when ℓ and λ are large, it costs more free energy to decrease ℓ than it does to decrease λ.

Eq. **9** shows that decreasing the density causes ρ, the fraction of the system in the striped phase, to decrease, with $\rho = 0$ for

densities less than $2\sqrt{3}\chi/3\ell^2$. When $\rho = 0$, the system is in the disordered hexagonal phase, with the typical hexagon side length ℓ dependent on the particle density.

To summarize the results in this section, we find that at very low densities the system is in the disordered hexagonal phase, whereas at higher density the system exhibits two-phase coexistence of stripes and disordered hexagons, with the size of the disordered hexagons independent of particle density.

Comparison with Experiment

In this section we compare simulation and analytical results with experimental data. Fig. 4 shows metastable images from a linear sequence of images taken during a compression from the mesh network hash stage until the thin lines congregate into thick trilayer bands. The progression of images is qualitatively similar to that yielded by simulation of the model with parameter values given in Fig. 4. Fig. 4 compares the images from the experiment (Fig. 4 *A*, *C*, *E*, and *G*) with images from the simulation (Fig. 4 *B*, *D*, *F*, and *H*); Fourier transforms (FFTs) of the images are also shown in Fig. 4.

The observed qualitative trends in the experiment (hash at low density and coexistence of hash and dense regions of many lines) are consistent with those exhibited by the model at thermal equilibrium. However, it is likely that the experimental configurations are not in thermal equilibrium—they are visibly anisotropic, and direct observation of the system does not yield evidence of configurational rearrangement at long times. We hypothesize that the kinetics are significantly faster in the initial stages of fold formation, so that significant relaxation occurs on short timescales, but the kinetics then arrest, and at long times the configurations are frozen. To investigate the robustness of the qualitative features when thermal equilibrium is not reached, we also investigated the configurations of the model in which the initial configuration is a uniform array of lines and the system evolves via Monte Carlo dynamics for a relatively short time.

Examination of Fig. 4 shows the similarity between the results of our simulation and the experiment as the density is changed (in the experiment this is done by increasing the compression). Although the FFTs from both systems are fundamentally different due to the pixelation (rectangular grid vs. hexagonal), they undergo similar transitions as a function of density (and also vertex energy, as shown in Fig. 5).

Fig. 5 shows the early metastable stages of a compression from a configuration with straight and parallel hash lines to a configuration with intersecting and disordered hash lines and (Fig. 5 *B*, *D*, and *F*) shows qualitatively similar configurations from
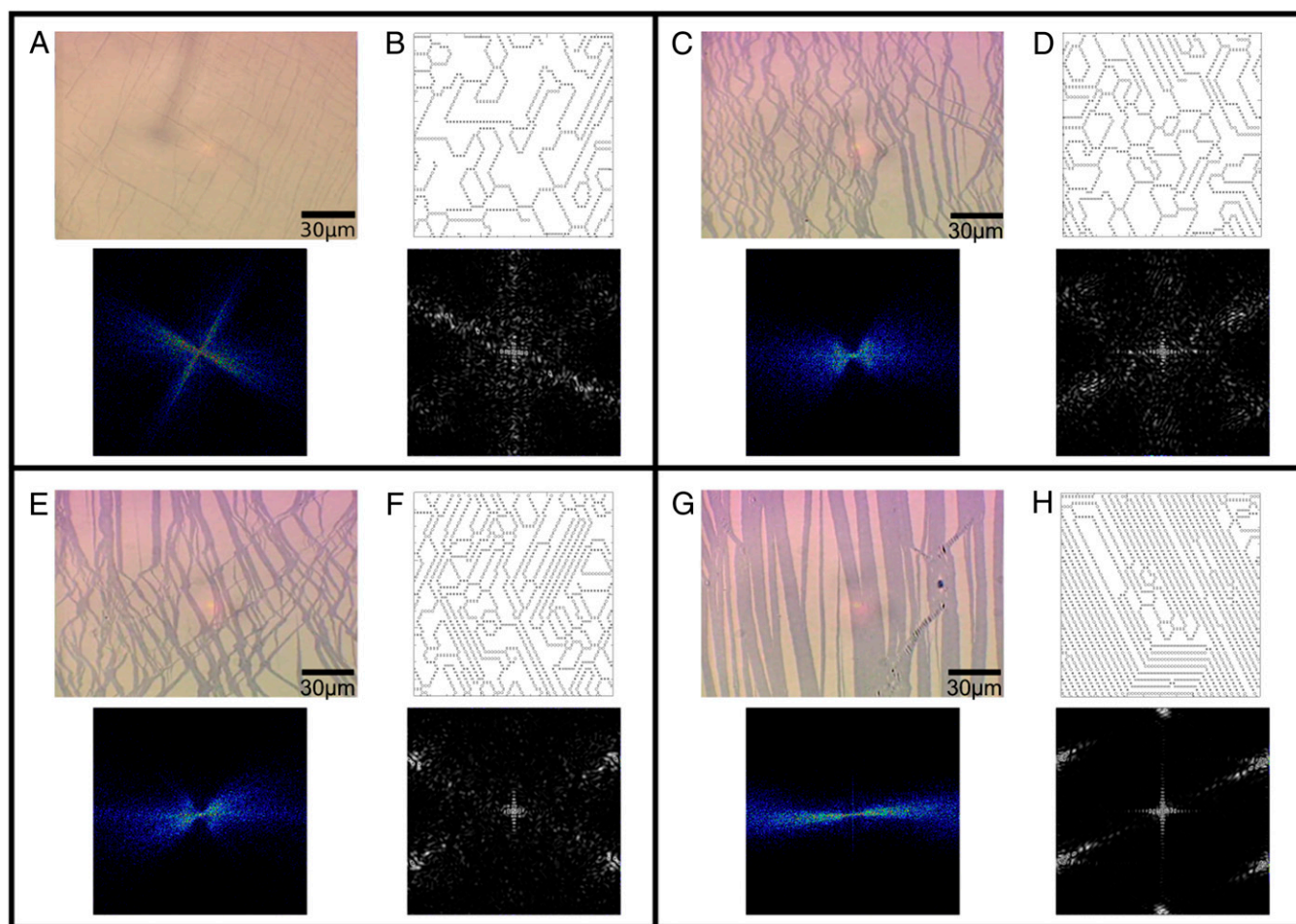
Fig. 4. Image comparisons between configurations observed in the experiment and Monte Carlo configurations in the simulation. The experiment was performed at room temperature with 6-nm gold nanoparticles. The simulations were done in a 60×60-cell grid with $\frac{1}{k_B T} = 0.135$ over a period of 6×10^8 Monte Carlo steps (MCS) with $E = E_f k_B T$, where $\vec{E}_f$ is the vector of parameter values defined in *Materials and Methods*. (*A* and *B*) The mesh network of thin "hash" lines (*A*) demonstrates good qualitative agreement with the disordered hexagonal phase in the simulation (*B*) (density = 0.20). (*C*) The film in the experiment responds to further compression by congregating the thin trilayer lines into thick bands. (*D*) In the simulation the density is increased to 0.25. (*E*) Further compression in the experiment causes the trilayer bands to increase in width and straighten out, which is mirrored in *F* by increasing the density to 0.33. (*G*) As it approaches the end of the hash stage the experiment is characterized by thick hash bands. (*H*) In the simulation, increasing the density to 0.44 achieves a similar result. In each panel, real-space images are shown above the corresponding fourier-transform (FFT) for both experiment and simulation.

the simulation. We compare the experimental configurations (Fig. 5 *A*, *C*, and *E*) to unequilibrated Monte Carlo systems with different densities. In the experiment, compressing the film causes the trilayer lines to intersect and bend (Fig. 5 *C* and *E*). By comparing the simulation across different densities (Fig. 5 *B*, *D*, and *F*), we demonstrate good qualitative agreement with the experiment as the density increases through compression. In the simulations, a lower density of particles leads to a striped phase, whereas higher density leads to a disordered hexagonal phase after the same amount of average movements across all particles.

We also performed experiments to search for direct evidence of thermally induced line rearrangements, using two different experimental procedures. The first is a quasi-static approach where the film is compressed in incremental units of area while the film sits for a period (500 s) in between compressions. The surface pressure and images from the start and the end of a stationary period shown in Fig. S2 show a relaxation in the pressure when compression is stopped due to the release of pressure built up during the compression (28), but rearrangement of nanoparticles was not observed.

In the second experiment, the film is compressed until hash lines appear and then the film sits for a very long period (16 h).

There is no visual evidence (Fig. S3) of structural changes in the film even after 16 h. This absence of observable variability at long times may be due to changes in the characteristic rearrangement times as the trilayer ages. Further experiments are needed to characterize the processes that govern the dynamics of trilayer rearrangements. In particular, adding excess ligand to the particle solution could have significant effects both on the width of the hash lines and on their kinetics (11, 28).

Summary

In this paper we describe the behavior of the metastable hash stage of trilayer lines forming disordered intersections under uniaxial compression by applying a thermodynamic equilibrium model, using lines that can wander and intersect. The model exhibits a disordered hexagonal phase when the particle density is low enough. At higher particle densities, the model exhibits two-phase coexistence of a disordered hexagonal phase and a phase of dense stripes. We show that the nature of behavior as the density is increased is qualitatively similar to experimental measurements of a gold nanoparticle film as it is compressed. Experimentally, lower degrees of compression yield hash configurations with properties that are qualitatively very similar to those of the
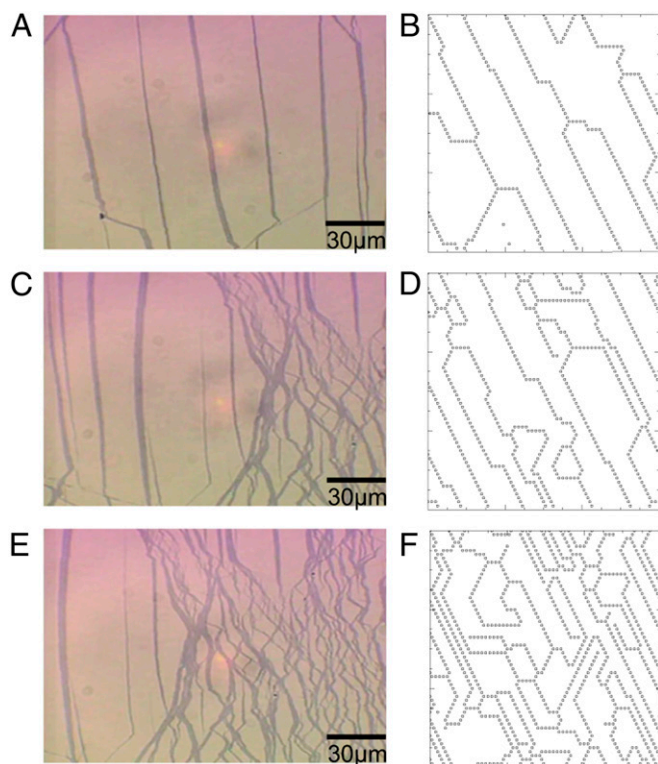
Chua et al.

Fig. 5. Comparison between the early stages of compression in the experiment and simulations performed with different densities. The experiment was performed at room temperature with 6-nm gold nanoparticles. The simulation was done in a 60 × 60-cell grid with $\frac{1}{k_B T} = 0.135$ and $E = E_f k_B T$, where the vector of parameters $\vec{E}_f$ is defined in *Materials and Methods*. (*A*) Very early stage of the compression characterized by straight parallel "hash" lines. (*B*) In the simulation we started with the initial condition of straight parallel lines at particle density of 0.10. *B* shows a configuration obtained after the particles have experienced an average of 3×10^5 movements each when this snapshot is taken and compared with the experimental image in *A*. (*C*) Further compression in the experiment causes the hash lines to wander and intersect. (*D*) By increasing the density to 0.15 in the simulation, a snapshot of the configuration is taken after around 6×10^5 per particle and compared with the experimental image in *K*. (*E*) At this stage of compression, the criss-crossing hash lines become dominant. (*F*) Simulation configuration obtained after 4×10^5 moves per particle at a density of 0.25, in which disordered hexagons are apparent.

disordered hexagonal phase. As the density of lines is increased by further compression of the film, we observe a coexistence of hash and thick bands of closely spaced lines. Again, this behavior is qualitatively consistent with that exhibited by the theoretical model. Thus, we have shown that a free energy model formulated in terms of the meandering and intersecting of lines is qualitatively consistent with the behavior of gold nanoparticle films undergo uniaxial compression (11).

Materials and Methods

Experiment. This section presents the experimental methods of a Langmuir monolayer compression at an interface. A Langmuir film of 6-nm gold nanoparticles ligated with dodecanethiol (Ocean Nanotech) and suspended in heptane is spread at the air–water interface of a $(15 \times 7) \text{cm}^2$ Langmuir trough (Nima Technology) with two barriers. The film is then allowed to rest for 15–20 min to evaporate off the heptane and then imaged continuously for the duration of the compression, using an optical microscope.

The trough, made from a single piece of Teflon polytetrafluoroethylene (PTFE) so that it is chemically inert and hydrophobic, is vibration isolated to stabilize the monolayer. Teflon barriers at the water–air interface are used to compress the monolayer laterally. Pure water (resisitivity 18.2 MΩ – cm) is used to fill the trough. A single Wilhelmy plate attached to a sensor is used

to measure the surface pressure as a result of the compression of the monolayer.

The trough and barriers are cleaned by solvents (chloroform and acetone) multiple times, and the water subphase is then added until the meniscus reaches the barrier. The surface is then aspirated to remove impurities. Once the surface is ready for nanoparticle spreading, a Hamilton microsyringe is used to deposit the nanoparticles by small drops that disperse throughout the surface as the drops are lowered slowly to touch the surface.

Monte Carlo Simulation. This section describes the construction and programming of the Monte Carlo simulation. The model is constructed on a hexagonal grid, using periodic boundary conditions and two dimensions, x and y. Each particle of excess density is described using an (i, j) coordinate pair, as shown in Fig. 6. At the boundaries, if any coordinate value i exceeds associated dimension x or returns a negative integer, i will be shifted by x, such that i is within the bounds $[0, x)$.

The energy of the model is written as the sum of the energies of all local regions, where each local region is defined as any given cell plus the six immediately adjacent cells, as seen in Fig. 6. The energy of each local region is determined by the occupied central cell and the distribution of the surrounding occupied cells, with the energies determined by the parameters shown in Fig. 7.

The energy parameters in the model are chosen such that the minimum energy configuration on small scales consists of continuous straight lines, whereas "clusters," or nonlinear collections of particles, are energetically disfavored (Fig. 7 *E* and *G–K*). We explored specifically the effects of changing parameter governing the local energy of intersections (Fig. 7*F*), focusing on the region in the parameter space in which there existed a transition between hexagons and lines, and found the critical vertex energy where phase coexistence occurs. Other parameters for this model include the number of cells N, the density, defined as the fraction of occupied cells in the entire x by y hexagonal grid, and the inverse temperature parameter $\frac{1}{k_B T}$.

We define the energy parameter $\vec{E}$ as the set

$$\cup E_\chi = \{ E_{\chi_1}, E_{\chi_2}, \ldots E_{\chi_n} \},$$

where each χ is a six-bit string corresponding to a unique arrangement of the six occupied and unoccupied cells neighboring a central occupied location, starting at the $(i, j + 1)$ location in Fig. 6 and rotating counterclockwise. As an example, the string representation of Fig. 7*F* is "010101," and that of
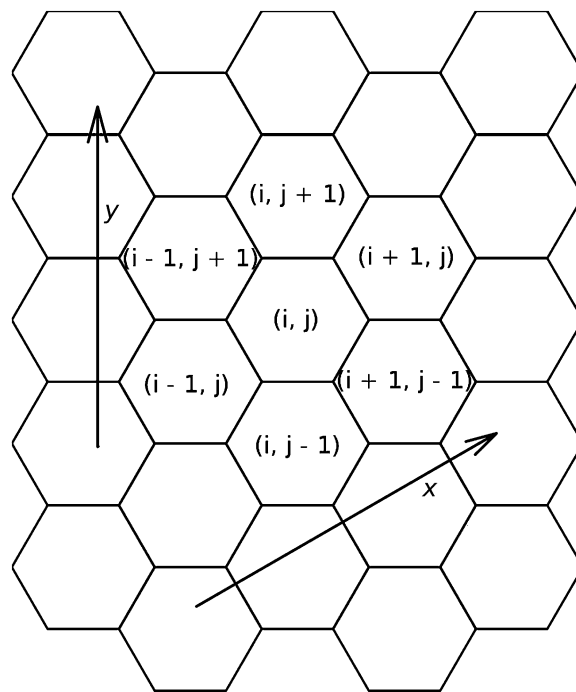
Fig. 6. The coordinate system for the simulation model. Periodic boundary conditions are implemented in the two directions indicated by the arrows. Also note that i is the x-component in this system, with j the corresponding y-component.
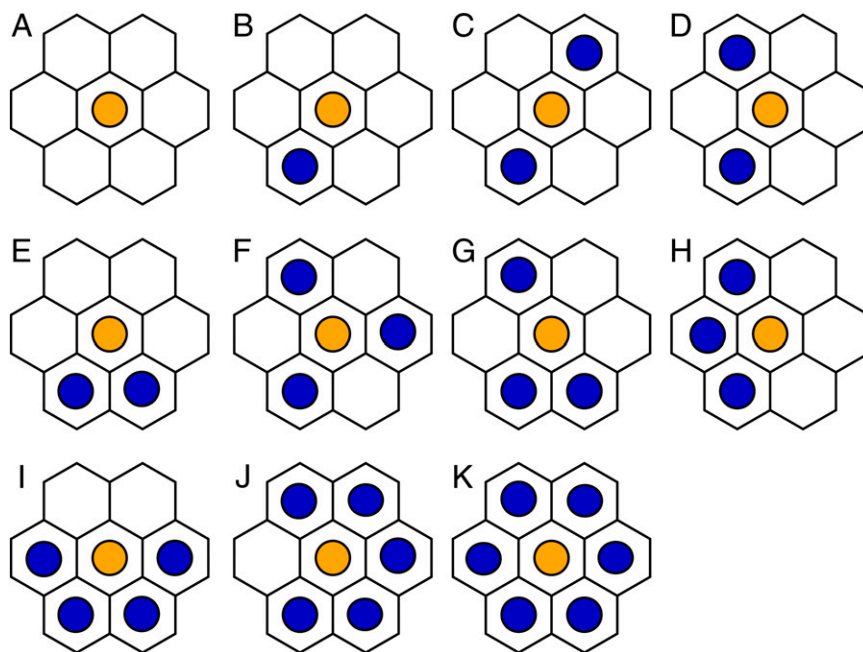
Fig. 7. Definition of energy functional for model investigated in the Monte Carlo simulations. The total energy is written as the sum of energies of local regions consisting of seven hexagonal cells. The energies of the local regions are chosen so that configurations with straight lines have the lowest energy. (*A*) The configuration is represented by the string "000000." (*B*) The configuration is represented by the string "000100." (*C–K*) Configurations are (*C*) "100100" (straight line configuration), (*D*) "010100," (*E*) "000110," (*F*) "010101" (vertex configuration), (*G*) "010110," (*H*) "011100," (*I*) "001111," (*J*) "110111," and (*K*) "111111."

Fig. 7*G* is "010110." The energy of a configuration α of the local cell is taken to be rotationally invariant (e.g., the configuration 010110 is energetically identical to 101100).

In the simulation, we represent all possible configurations as some χ_n: $\chi_1 = 000000$, $\chi_2 = 000001$, $\chi_3 = 000011$, $\chi_4 = 000101$, $\chi_5 = 001001$, $\chi_6 = 000111$, $\chi_7 = 001011$, $\chi_8 = 010011$, $\chi_9 = 010101$, $\chi_{10} = 001111$, $\chi_{11} = 010111$, $\chi_{12} = 011011$, $\chi_{13} = 011111$, and $\chi_{14} = 111111$.

The value of the energy parameters used in the simulations shown in the main text can be written as $\vec{E} = \{74.179, 57.814, 42.604, 27.216, 10.124, 44.668, 49.037, 61.533, E_{010101}, 46.793, 49.588, 50.899, 46.619, 57.550\}$. With reference to Figs. 4 and 5, the vector of parameters $\vec{E}_f$ has value $E_{010101} = 18.204$.

The Monte Carlo simulations are performed using standard techniques (39); in each step, a random particle is chosen and a trial move to an un-occupied neighboring position is selected at random. The change in energy obtained when the trial move is made is calculated from the sum of the energies of the original and new cells of the particle, along with the energies of the shared neighboring cells within the lattice, both before and after the proposed move. The move is accepted using the usual Boltzmann criteria: If the energy is lowered, the move is accepted, and if the move raises the energy by ΔE, the move is accepted with probability $e^{-\frac{1}{k_B T}\Delta E}$.

Equilibration of the model was checked by starting from two different initial conditions (random initial placement of particles and an organized line lattice) and comparing both the total energy and the qualitative nature of the configurations; the equilibration time is estimated to be the time at which the system energy and spacial correlation functions become independent of the choice of starting configurations.

1. Ries HE, Jr., Kimball WA (1955) Monolayer structure as revealed by electron microscopy. *J Phys Chem* 59(1):94–95.
2. Ries HE, Jr., Kimball WA (1958) Electron micrographs of monolayers of stearic acid. *Nature* 181:901–901.
3. Genzer J, Groenewold J (2006) Soft matter with hard skin: From skin wrinkles to templating and material characterization. *Soft Matter* 2:310–323.
4. Böker A, et al. (2004) Hierarchical nanoparticle assemblies formed by decorating breath figures. *Nat Mater* 3(5):302–306.
5. Pocivavsek L, et al. (2008) Stress and fold localization in thin elastic membranes. *Science* 320(5878):912–916.
6. Lu W, Knobler CM, Bruinsma RF, Twardos M, Dennin M (2002) Folding Langmuir monolayers. *Phys Rev Lett* 89(14):146107–146110.
7. Vella D, Bico J, Boudaoud A, Roman B, Reis PM (2009) The macroscopic delamination of thin films from elastic substrates. *Proc Natl Acad Sci USA* 106(27):10901–10906.
8. Zhang Q, Witten TA (2007) Microscopic wrinkles on supported surfactant monolayers. *Phys Rev E Stat Nonlin Soft Matter Phys* 76(4 Pt 1):041608–041618.
9. Milner ST, Joanny JF, Pincus P (1989) Buckling of Langmuir monolayers. *Europhys Lett* 9(5):495–500.
10. Vella D, Aussillous P, Mahadevan L (2004) Elasticity of an interfacial particle raft. *Europhys Lett* 68(2):212–218.
11. Leahy BD, et al. (2010) Geometric stability and elastic response of a supported nanoparticle film. *Phys Rev Lett* 105(5):058301–058304.

12. Zasadzinski JA, Ding J, Warriner HE, Bringezu F, Waring AJ (2001) The physics and physiology of lung surfactants. *Curr Opin Colloid Interface Sci* 6:506–513.
13. Pocivavsek L, et al. (2008) Lateral stress relaxation and collapse in lipid monolayers. *Soft Matter* 4:2019–2029.
14. Bu W, Vaknin D (2008) Bilayer and trilayer crystalline formation by collapsing behenic acid monolayers at gas/aqueous interfaces. *Langmuir* 24(2):441–447.
15. Vaknin D, Bu W, Satija SK, Travesset A (2007) Ordering by collapse: Formation of bilayer and trilayer crystals by folding Langmuir monolayers. *Langmuir* 23(4):1888–1897.
16. Coppersmith SN, Fisher DS, Halperin BI, Lee PA, Brinkman WF (1981) Dislocations and the commensurate-incommensurate transition in 2 dimensions. *Phys Rev Lett* 46(8):549–552.
17. Coppersmith SN, Fisher DS, Halperin BI, Lee PA, Brinkman WF (1982) Dislocations and the commensurate-incommensurate transition in 2 dimensions. *Phys Rev B* 25(1):349–363.
18. Bak P, Mukamel D (1979) Phase-transitions in 2-dimensionally modulated systems. *Phys Rev B* 19(3):1601–1609.
19. Frank FC, van der Merwe JH (1949) One-dimensional dislocations. I. Static theory. *Proc R Soc London Ser A* 198:205–216.
20. Frank FC, van der Merwe JH (1949) One-dimensional dislocations. II. Misfitting monolayers and oriented overgrowth. *Proc R Soc London Ser A* 198:216–225.
21. Bak P, Mukamel D, Villain J, Wentowska K (1979) Commensurate-incommensurate transitions monolayers adsorbed on graphite and in layered charge-density-wave systems. *Phys Rev B* 19(3):1610–1613.

Chua et al.

22. Pokrovsky VL, Talapov AL (1979) Ground-state, spectrum, and phase-diagram of 2-dimensional incommensurate crystals. *Phys Rev Lett* 42(1):65–67.
23. Fisher ME, Fisher DS (1982) Wall wandering and the dimensionality dependence of the commensurate-incommensurate transition. *Phys Rev B* 25(5):3192–3198.
24. Villain J (1980) Two-dimensional solids and their interaction with substrates. *Ordering in Strongly Fluctuating Systems*, ed Riste T (Plenum, New York), pp 221–260.
25. Bruch LW (1993) Elastic continuum theory of the structure and dynamics of uniaxially incommensurate monolayer solids. *Phys Rev B Condens Matter* 48(3):1765–1778.
26. Bruch LW, Diehl RD, Venables JA (2007) Progress in the measurement and modeling of physisorbed layers. *Rev Mod Phys* 79(4):1381–1454.
27. Stephens PW, Heiney P, Birgeneau RJ, Horn PM (1979) X–ray scattering study of the commensurate-incommensurate transition of monolayer krypton on graphite. *Phys Rev Lett* 43(1):47–51.
28. Schultz DG, et al. (2006) Structure, wrinkling, and reversibility of Langmuir monolayers of gold nanoparticles. *J Phys Chem B* 110(48):24522–24529.
29. Abraham FF, Koch SW, Rudge WE (1982) Molecular-dynamics computer-simulation of the weakly incommensurate phase of monolayer krypton on graphite. *Phys Rev Lett* 49(25):1830–1833.
30. McMillan WL (1976) Theory of discommensurations and commensurate-incommensurate charge-density wave-phase transition. *Phys Rev B* 14(4):1496–1502.
31. Bak P, Emery VJ (1976) Theory of structural phase-transformations in tetrathiafulvalene-tetracyanoquinodimethane (TTF–TCNQ). *Phys Rev Lett* 36(16):978–982.
32. Lobkovsky AE, Witten TA (1997) Properties of ridges in elastic membranes. *Phys Rev E Stat Phys Plasmas Fluids Relat Interdiscip Topics* 55(2):1577–1589.
33. Abraham FF, Rudge WE, Auerbach DJ, Koch SW (1984) Molecular-dynamics simulations of the incommensurate phase of krypton on graphite using more than 100000 atoms. *Phys Rev Lett* 52(6):445–448.
34. Koch SW, Abraham FF (1983) Molecular-dynamics simulations of phase-.transitions in physisorbed noble gases. *Helv Phys Acta* 56(1–3):755–764.
35. Koch SW, Rudge WE, Abraham FF (1984) The commensurate incommensurate transition of krypton on graphite – a study via computer-simulation. *Surf Sci* 145(2–3):329–344.
36. Selke W (1984) Monte-Carlo studies on commensurate incommensurate transitions. *Surf Sci* 144(1):89–91.
37. Parsonage NG (1992) Monte-Carlo studies of a 2-dimensional commensurate incommensurate system - effects of change of particle-size and interaction parameters at constant number density. *J Chem Soc, Faraday Trans* 88(6):777–787.
38. Flenner E, Etters RD (2006) Properties of argon adlayers deposited on graphite from Monte Carlo calculations. *Phys Rev B* 73(12):125419–125428.
39. Gould H, Tobochnik J, Christian W (2007) *Introduction to Computer Simulation Methods: Applications to Physical Systems* (Addison–Wesley, Reading, MA), 3rd Ed.

Supporting Information

Chua et al. 10.1073/pnas.1101630108

SI Text S1: Phenomenological Analysis of Two-Phase Coexistence

Here we present details of our analysis of the free energy of the system, demonstrating the presence of a region of two-phase coexistence. We first present the free energies of the striped and hexagonal phases separately and then show that there is a substantial regime of parameters in which two-phase coexistence is favored.

1. Striped Phase. We define f_S to be the free energy per unit area of the striped phase. There are two terms that contribute to the free energy of the striped phase, the energy of the particles and the contribution to the free energy that arises from the entropically generated repulsion of the lines. We let ϵ be the energy per unit length of line, so that the energy of a line is $y\epsilon$, where y is the length of the line, and λy is the "area" occupied by a line, where λ is the mean separation between lines. We calculate the particle energy per unit area as

$$\frac{particle\ energy}{unit\ area} = \frac{particle\ energy}{line} \cdot \frac{\#\ of\ lines}{unit\ area}. \qquad \textbf{[S1.1]}$$

Here we have

$$\frac{particle\ energy}{unit\ area} = (y\epsilon) \cdot \left(\frac{1}{\lambda y}\right), \qquad \textbf{[S1.2]}$$

so the energy contribution to the free energy is $\frac{\epsilon}{\lambda}$.

The second, entropic, term arises from the entropic repulsion between lines, which scales as $1/\lambda^3$ (1, 2). Therefore, the entropic term in the free energy per unit area is $\frac{\eta k_B T}{\lambda^3}$. Combining the two terms, the total free energy per unit area of the striped phase is

$$f_S = \frac{\epsilon}{\lambda} + \frac{\eta k_B T}{\lambda^3}, \qquad \textbf{[S1.3]}$$

where ϵ is the energy per unit length and η is a constant.

2. Hexagonal Phase. The free energy per unit area of the hexagonal phase, which we denote as f_H, can be written in terms of the mean side length of the hexagon, ℓ. There are three terms that contribute to the free energy of the hexagonal phase, the energy of the particles, energy cost of each vertex, and the entropic term resulting from the entropic breathing of the hexagons. The first term can be derived from ϵ, the particle energy per unit length. A hexagon of side length ℓ has a perimeter of 6ℓ and energy of $6\ell\epsilon$. Because each side is shared by two hexagons, the line length per hexagon in a hexagonal array is $3\ell\epsilon$. Because the area of each hexagon is $\frac{3\sqrt{3}}{2}\ell^2$, the particle energy per unit area is

$$\frac{particle\ energy}{unit\ area} = \frac{particle\ energy}{hexagon} \cdot \frac{\#\ of\ hexagons}{unit\ area}$$

$$= (3\ell\epsilon) \cdot \left(\frac{2}{3\sqrt{3}\ell^2}\right)$$

$$= \frac{2\epsilon}{\sqrt{3}\ell}. \qquad \textbf{[S1.4]}$$

The second term is contributed by the energy cost of intersections per unit area. Each hexagon has six intersections. Because each intersection is shared by three hexagons, there are two intersections per hexagon. Therefore, letting E_V be the energy of

an intersection, each hexagon has $2E_V$ in vertex energy. Using the area of a hexagon, $\frac{3\sqrt{3}}{2}\ell^2$, we can calculate the vertex energy through the following:

$$\frac{vertex\ energy}{unit\ area} = \frac{vertex\ energy}{hexagon} \cdot \frac{\#\ of\ hexagons}{unit\ area}$$

$$= (2E_V) \cdot \left(\frac{2}{3\sqrt{3}\ell^2}\right)$$

$$= \frac{4E_V}{3\sqrt{3}\ell^2}. \qquad \textbf{[S1.5]}$$

The third term is caused by the entropy from the "breathing" of the hexagons, which scales as $\frac{\ln \ell/a}{\ell^2}$ (3–5). So the third term is just $-\frac{k_B T}{\ell^2} \ln \frac{\ell}{a}$, where a is the microscopic length setting the minimum spatial variation scale. Putting the three terms together we get the total free energy per unit area of the hexagonal phase,

$$f_H = \frac{4\epsilon}{3\sqrt{3}\ell} + \frac{2E_V}{\sqrt{3}\ell^2} - \frac{k_B T}{\ell^2} \ln\left(\frac{\ell}{a}\right), \qquad \textbf{[S1.6]}$$

where ϵ is the number of particles per unit length and E_V is the intersection energy.

3. Phase Coexistence. When there is phase coexistence, the total free energy per unit area is just the appropriate weighted sum of the free energy of two phases. Letting ρ be the fraction of the area that is in the striped phase, the total energy per unit area is

$$f_{S+H} = \rho\left(\frac{\epsilon}{\lambda} + \frac{\eta k_B T}{\lambda^3}\right) + (1-\rho)\left(\frac{2\epsilon}{\sqrt{3}\ell} + \frac{4E_V}{3\sqrt{3}\ell^2} - \frac{k_B T}{\ell^2} \ln\left(\frac{\ell}{a}\right)\right). \qquad \textbf{[S1.7]}$$

3.1. Constraint. We also have to implement the constraint that the total number of particles is fixed. Let σ be the total number of particles in the system. In the striped phase, we can calculate the number of particles per unit area through

$$\frac{\#\ of\ particles}{unit\ area} = \frac{\#\ of\ particles}{line} \cdot \frac{\#\ of\ lines}{unit\ area}$$

$$= (y\chi) \cdot \left(\frac{1}{\lambda y}\right)$$

$$= \frac{\chi}{\lambda}, \qquad \textbf{[S1.8]}$$

where χ is the number of particles per unit length (i.e., the line density). Note that this is the same form as Eq. **S1.2** except the energy per unit length has been replaced by the number of particles per unit length.

For the hexagonal phase, we can calculate the number of particles per unit area through the following:

$$\frac{\text{\# of particles}}{\text{unit area}} = \frac{\text{\# of particles}}{\text{hexagon}} \cdot \frac{\text{\# of hexagons}}{\text{unit area}}$$

$$= (3\ell\chi) \cdot \left(\frac{2}{3\sqrt{3}\ell^2}\right)$$

$$= \frac{2\chi}{\sqrt{3}\ell}. \qquad \textbf{[S1.9]}$$

Given that ρ is the portion of the striped phase, the total constraint is

$$\sigma = \rho\frac{\chi}{\lambda} + (1-\rho)\frac{2\chi}{\sqrt{3}\ell}. \qquad \textbf{[S1.10]}$$

4. Minimizing the Free Energy. Putting everything together and introducing a Lagrange multiplier ζ, we write the free energy per unit area of the system $\mathcal{F}$ as

$$\mathcal{F} = \rho\left(\frac{\epsilon}{\lambda} + \frac{\eta k_B T}{\lambda^3}\right) + (1-\rho)\left(\frac{2\epsilon}{\sqrt{3}\ell} + \frac{4E_V}{3\sqrt{3}\ell^2} - \frac{k_B T}{\ell^2}\ \ln\ \left(\frac{\ell}{a}\right)\right)$$

$$+ \zeta\left(\sigma - \rho\frac{\chi}{\lambda} - (1-\rho)\frac{2\chi}{\sqrt{3}\ell}\right), \qquad \textbf{[S1.11]}$$

where the Lagrange multiplier ζ is determined by the implementation of the constraint Eq. **S1.10**.

We can solve for the minimum of the free energy by taking the partial with respect to the three parameters, λ, ℓ, and ρ. We find

$$\ell = \frac{\sqrt{3}k_B T \ln\left(\frac{\ell}{a}\right) - \frac{4E_V}{3} - \frac{\sqrt{3}k_B T}{2}}{\epsilon - \chi\zeta}, \qquad \textbf{[S1.15]}$$

$$\frac{\partial \mathcal{L}}{\partial \zeta} = \sigma - \rho\frac{\chi}{\lambda} - (1-\rho)\frac{2\chi}{\sqrt{3}\ell} = 0, \qquad \textbf{[S1.16]}$$

$$\rho = \frac{\lambda(3\ell\sigma - 2\sqrt{3}\chi)}{\chi(3\ell - 2\sqrt{3}\lambda)}, \qquad \textbf{[S1.17]}$$

$$\frac{\partial \mathcal{L}}{\partial \rho} = \frac{\epsilon}{\lambda} + \frac{\eta k_B T}{\lambda^3} - \frac{2\epsilon}{\sqrt{3}\ell} - \frac{4E_V}{3\sqrt{3}\ell^2} + \frac{k_B T}{\ell^2}\ln\left(\frac{\ell}{a}\right) - \frac{\zeta\chi}{\lambda} + \frac{2\chi\zeta}{\sqrt{3}\ell} = 0, \qquad \textbf{[S1.18]}$$

$$\frac{\epsilon - \zeta\chi}{\lambda} + \frac{\eta k_B T}{\lambda^3} = \frac{\frac{4E_V}{3\sqrt{3}} - k_B T \ln\left(\frac{\ell}{a}\right)}{\ell^2} + \frac{2\epsilon - 2\chi\zeta}{\sqrt{3}\ell}. \qquad \textbf{[S1.19]}$$

Rearranging these equations yields the results

$$\zeta = \frac{\epsilon}{\chi} + \frac{3\eta k_B T}{\lambda^2 \chi} = \frac{\sqrt{3}}{2\chi\ell}\left(\frac{2\epsilon\ell}{\sqrt{3}} - 2k_B T \ln\left(\frac{\ell}{a}\right) + \frac{8}{3\sqrt{3}}E_V + k_B T\right), \qquad \textbf{[S1.20]}$$

$$\ell = \frac{54\sqrt{3}\eta k_B T \left(4\sqrt{3}E_V - 9k_B T\left(\ln\left(\frac{\ell}{a}\right) - 1\right)\right)^2}{\left(8\sqrt{3}E_V - 9k_B T\left(2\ln\ \left(\frac{\ell}{a}\right) - 1\right)\right)^3}, \qquad \textbf{[S1.21]}$$

$$\lambda^2 = \frac{18\sqrt{3}\eta k_B T\ell}{8\sqrt{3}E_V - 9k_B T\left(2\ln\left(\frac{\ell}{a}\right) - 1\right)} = \frac{18\sqrt{3}\eta k_B T}{8\sqrt{3}E_V - 9k_B T\left(2\ln\left(\frac{\ell}{a}\right) - 1\right)}\frac{54\sqrt{3}\eta k_B T\left(4\sqrt{3}E_V - 9k_B T\left(\ln\left(\frac{\ell}{a}\right) - 1\right)\right)^2}{\left(8\sqrt{3}E_V - 9k_B T\left(2\ln\left(\frac{\ell}{a}\right) - 1\right)\right)^3}$$

$$= \frac{2,916(\eta k_B T)^2\left(4\sqrt{3}E_V - 9k_B T\left(\ln\left(\frac{\ell}{a}\right) - 1\right)\right)^2}{\left(8\sqrt{3}E_V - 9k_B T\left(2\ln\left(\frac{\ell}{a}\right) - 1\right)\right)^4}, \qquad \textbf{[S1.22]}$$

$$\frac{\partial \mathcal{L}}{\partial \lambda} = \rho\left(\frac{-\epsilon}{\lambda^2} - \frac{3\eta k_B T}{\lambda^4}\right) + \zeta\left(\frac{\rho\chi}{\lambda^2}\right) = 0, \qquad \textbf{[S1.12]}$$

$$\lambda^2 = \frac{3\eta k_B T}{\zeta\chi - \epsilon}, \qquad \textbf{[S1.13]}$$

$$\frac{\partial \mathcal{L}}{\partial \ell} = (1-\rho)\left(-\frac{2\epsilon}{\sqrt{3}\ell^2} - \frac{8E_V}{3\sqrt{3}\ell^3} + \frac{2k_B T}{\ell^3}\ln\left(\frac{\ell}{a}\right) - \frac{k_B T}{\ell^3}\right)$$
$$+ \zeta\left((1-\rho)\frac{2\chi}{\sqrt{3}\ell^2}\right) = 0, \qquad \textbf{[S1.14]}$$

$$\rho = \frac{\lambda(3\ell\sigma - 2\sqrt{3}\chi)}{\chi(3\ell - 2\sqrt{3}\lambda)}. \qquad \textbf{[S1.23]}$$

The hexagon side length ℓ is independent of particle density and is dependent on the external parameters and constants of the system only. We can also reduce the scaling of λ:

$$\lambda^2 \sim \frac{\left(1 - \left(\ln\left(\frac{\ell}{a}\right) - 1\right)\right)^2}{\left(2 - \left(2\ln\left(\frac{\ell}{a}\right) - 1\right)\right)^4}$$

$$\sim \frac{\left(\ln\left(\frac{\ell}{a}\right) - 2\right)^2}{\left(2\ln\left(\frac{\ell}{a}\right) - 3\right)^4}$$

$$\rightarrow \frac{1}{\left(\ln\left(\frac{\ell}{a}\right)\right)^2} \text{ in the limit as } \ell\rightarrow\infty. \qquad \textbf{[S1.24]}$$

5. Discussion. Here we determine the regime in which phase co-existence occurs. Phase coexistence exists when $0 < \rho < 1$. So we first determine the regime where $\rho > 0$ and then determine where $\rho < 1$. Using Eq. **S1.23**, one finds that the fraction of striped phase, ρ, is greater than zero when one of the following two conditions is true:

$$\ell > \frac{2\sqrt{3}\chi}{3\sigma} \quad and \quad \ell > \frac{2\sqrt{3}\lambda}{3}$$

or

$$\ell < \frac{2\sqrt{3}\chi}{3\sigma} \quad and \quad \ell < \frac{2\sqrt{3}\lambda}{3}. \qquad \textbf{[S1.25]}$$

The fraction of striped phase, ρ, is less than one, $\frac{\lambda(3\ell\sigma - 2\sqrt{3}\chi)}{\chi(3\ell - 2\sqrt{3}\lambda)} = \rho < 1$, when

$$3\ell\chi - 2\sqrt{3}\chi\lambda > 3\ell\sigma\lambda - 2\sqrt{3}\chi\lambda \rightarrow \lambda < \frac{\chi}{\sigma}. \qquad \textbf{[S1.26]}$$

Combining Eqs. **S1.25** and **S1.26** we get the overall constraint for phase coexistence,

$$0 < \frac{\sqrt{3}\ell}{2} < \lambda < \frac{\chi}{\sigma} \quad or \quad \frac{\sqrt{3}\ell}{2} > \frac{\chi}{\sigma} > \lambda > 0. \qquad \textbf{[S1.27]}$$

Eq. **S1.27** can be interpreted in simple terms. As the density $\frac{\chi}{\sigma}$ increases, the average line separation in the striped phase, λ, decreases, which increases the portion of the striped phase because ρ scales with λ as $\rho \sim \frac{\ell\lambda\sigma - \chi\lambda}{\ell\chi - \chi\lambda}$. This result makes intuitive sense given the results of the simulations.

Recall that

$$\ell = \frac{54\sqrt{3}\eta k_B T \left(4\sqrt{3}E_V - 9k_B T\left(\ln\left(\frac{\ell}{a}\right) - 1\right)\right)^2}{\left(8\sqrt{3}E_V - 9k_B T\left(2\ln\left(\frac{\ell}{a}\right) - 1\right)\right)^3}, \qquad \textbf{[S1.21]}$$

$$\lambda^2 = \frac{2,916(\eta k_B T)^2 \left(4\sqrt{3}E_V - 9k_B T\left(\ln\left(\frac{\ell}{a}\right) - 1\right)\right)^2}{\left(8\sqrt{3}E_V - 9k_B T\left(2\ln\left(\frac{\ell}{a}\right) - 1\right)\right)^4}. \qquad \textbf{[S1.22]}$$

Applying Eq. **S1.27**, phase coexistence can occur only when

$$0 < \lambda^2 < \left(\frac{\chi}{\sigma}\right)^2$$

$$0 < \frac{2,916(\eta k_B T)^2 \left(4\sqrt{3}E_V - 9k_B T\left(\ln\left(\frac{\ell}{a}\right) - 1\right)\right)^2}{\left(8\sqrt{3}E_V - 9k_B T\left(2\ln\left(\frac{\ell}{a}\right) - 1\right)\right)^4} < \left(\frac{\chi}{\sigma}\right)^2. \qquad \textbf{[S1.28]}$$

Note that $\frac{2,916(\eta k_B T)^2 \left(4\sqrt{3}E_V - 9k_B T\left(\ln\left(\frac{\ell}{a}\right) - 1\right)\right)^2}{\left(8\sqrt{3}E_V - 9k_B T\left(2\ln\left(\frac{\ell}{a}\right) - 1\right)\right)^4} > 0$ always, due to the even power in the numerator and denominator.

1. Pokrovsky VL, Talapov AL (1979) Ground-state, spectrum, and phase-diagram of 2-dimensional incommensurate crystals. *Phys Rev Lett* 42(1):65–67.
2. Fisher ME, Fisher DS (1982) Wall wandering and the dimensionality dependence of the commensurate-incommensurate transition. *Phys Rev B* 25(5):3192–3198.
3. Coppersmith SN, Fisher DS, Halperin BI, Lee PA, Brinkman WF (1981) Dislocations and the commensurate-incommensurate transition in 2 dimensions. *Phys Rev Lett* 46(8):549–552.
4. Coppersmith SN, Fisher DS, Halperin BI, Lee PA, Brinkman WF (1982) Dislocations and the commensurate-incommensurate transition in 2 dimensions. *Phys Rev B* 25(1): 349–363.
5. Villain J (1980) Two-dimensional solids and their interaction with substrates. *Ordering in Strongly Fluctuating Systems*, ed Riste T (Plenum, New York), pp 221–260.
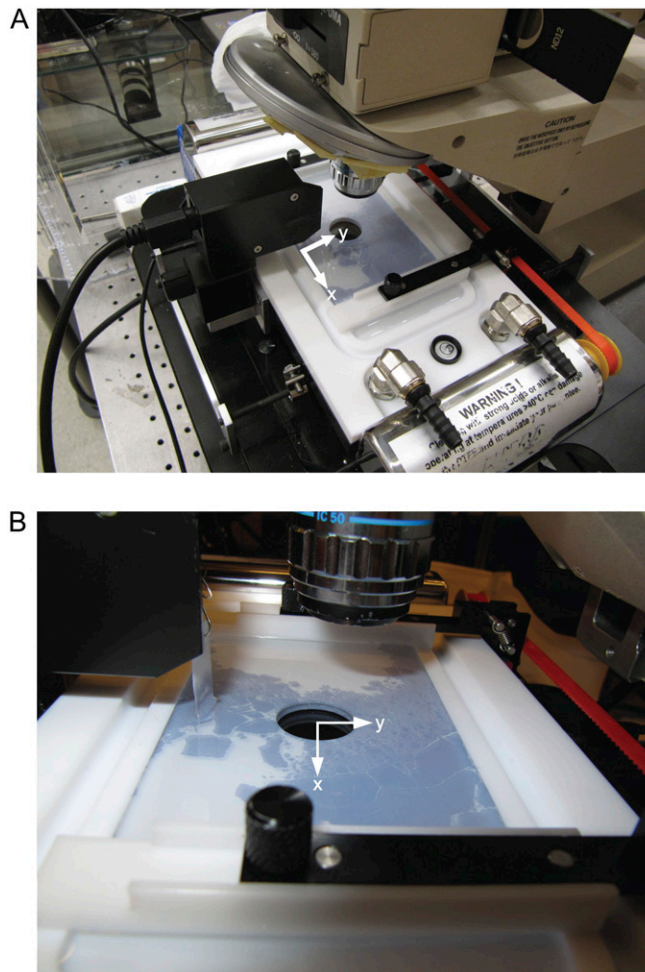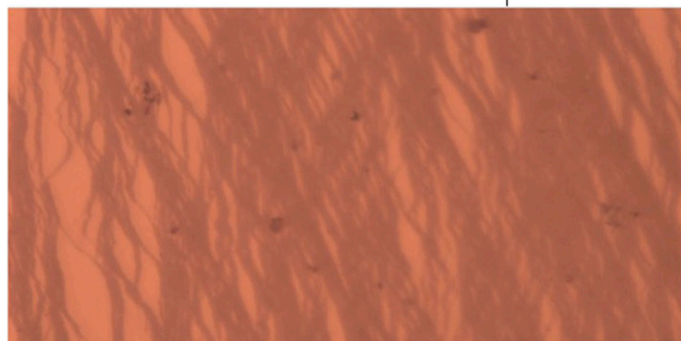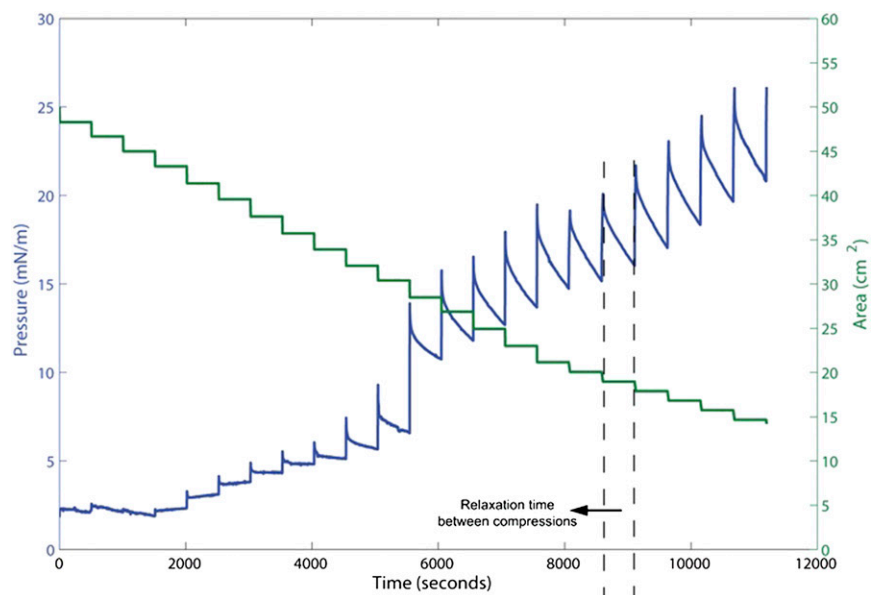
Fig. S1. Pictures of the experimental setup. *B* shows a close-up view of *A*. The strip of paper dipped in the trough acts as a Wilhelmy plate and is attached to a pressure sensor. The trough is filled with water with the gold nanoparticle monolayer forming blue islands the surface.

Fig. S2. Pressure and image data from a quasi-static compression. The experiment was performed at room temperature with 6-nm gold nanoparticles. The film was compressed by 1 cm^2 every 500 s. The surface image from the start of a stationary period looks indistinguishable from the surface image at the end of the same stationary period.
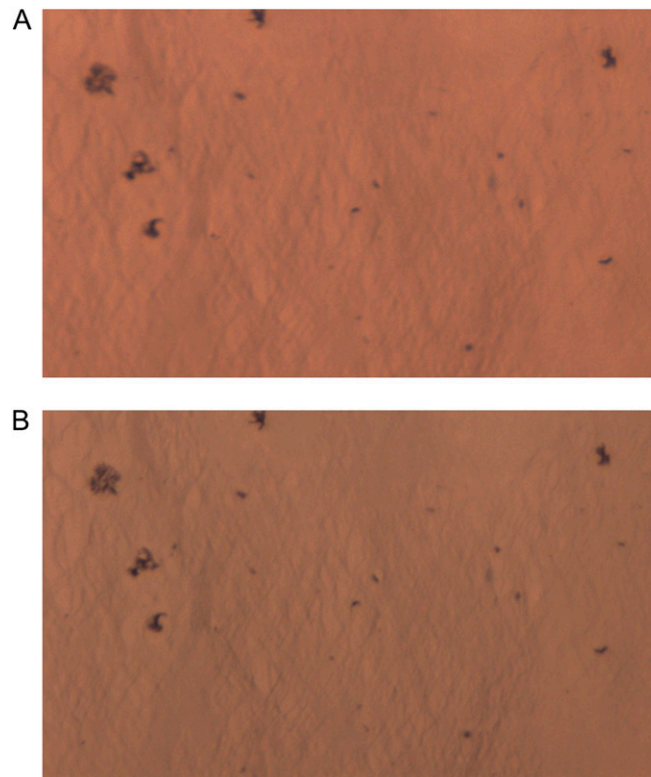
Fig. S3. Surface microscopy images from a long compression. (*A*) The surface configuration after compression is stopped. (*B*) The surface configuration after it has been sitting stationary for 16 h. No changes in the structure were detected.